RESEARCH ARTICLE

Discovery of Substituted 1,2,3-Triazolyl-Benzoylacetamides as Potent MMP-9 Inhibitors with Anti-Angiogenic Activity in MDA-MB-231 Triple-Negative Breast Cancer

Shaik Khasimbi, Sharad Wakode*

Dept. of Pharmaceutical chemistry, Delhi Institute of Pharmaceutical Sciences and Research (DIPSAR), DPSRU, Tughlakabad, New Delhi, Delhi-110017, India

ABSTRACT

Matrix metalloproteinase-9 (MMP-9) contributes to extracellular matrix remodeling, tumor invasion, and angiogenesis, making it an attractive therapeutic target for triple-negative breast cancer (TNBC). The present study aimed to develop non-hydroxamate MMP-9 inhibitors based on a substituted 1,2,3-triazolyl-benzoylacetamide scaffold and evaluate their antiproliferative and anti-angiogenic potentials. An energy-based, structure-guided pharmacophore approach was employed to define the key recognition features of the MMP-9 catalytic domain, including the catalytic Zn^{2+} environment and S1′ specificity pocket. A focused series of 13 derivatives (**8a–8m**) was subsequently designed through systematic modification of the benzoyl R^1 and terminal phenoxy R^2 regions, synthesized through a multistep route, and structurally characterized using spectroscopic and mass-spectrometric methods. The synthesized compounds exhibited concentration-dependent MMP-9 inhibition and antiproliferative activity against MDA-MB-231 cells, with the SAR analysis demonstrating a strong dependence on the combined steric, electronic, and lipophilic characteristics of R^1 and R^2. Compound **8h** emerged as the principal lead, whereas **8e** and **8l** also displayed favorable biochemical and cellular activity profiles. Morphological evaluation further supported the cellular effects of these active derivatives. Functional anti-angiogenic assessment demonstrated that **8h** concentration-dependently suppressed VEGF-induced HUVEC migration and disrupted capillary-like tube formation, approaching the activity of the reference anti-angiogenic agent at higher tested concentrations. Collectively, these findings identify substituted 1,2,3-triazolyl-benzoylacetamides as a promising non-hydroxamate chemotype for MMP-9-directed anti-angiogenic drug discovery and establish **8h** as a lead candidate for further mechanistic, selectivity, pharmacokinetic, and *in vivo* evaluations.

Keywords: MMP-9, 1,2,3-triazole, triple-negative breast cancer, MDA-MB-231, angiogenesis, HUVEC

How to cite this article: Shaik Khasimbi, Sharad Wakode. Discovery of Substituted 1,2,3-Triazolyl-Benzoylacetamides as Potent MMP-9 Inhibitors with Anti-Angiogenic Activity in MDA-MB-231 Triple-Negative Breast Cancer. International Journal of Drug Delivery Technology. 2026;16(80s):373-388. DOI: 10.25258/ijddt.16.80s.45.

Source of support: Nil.

Conflict of interest: None

INTRODUCTION

Triple-negative breast cancer (TNBC) is an aggressive and clinically challenging molecular subtype of breast cancer, characterized by the absence of estrogen receptor (ER), progesterone receptor (PR), and human epidermal growth factor receptor-2 (HER2). The lack of these canonical therapeutic targets restricts the applicability of endocrine and HER2-directed therapies and contributes to the dependence on chemotherapy, immunotherapy, antibody–drug conjugates and selected targeted approaches. TNBC is characterized by pronounced molecular heterogeneity, invasive behavior, early metastatic dissemination, and a highly dynamic tumor microenvironment. Importantly, aberrant neovascularization is a prominent component of TNBC progression, providing oxygen and nutrients to rapidly proliferating tumor cells while simultaneously establishing vascular routes for metastatic dissemination (Han et al., 2026). Tumor angiogenesis is orchestrated by coordinated interactions among malignant cells, endothelial cells, stromal components, the extracellular matrix (ECM), and soluble pro-angiogenic mediators. Vascular endothelial growth factor (VEGF) is a dominant angiogenic signal that promotes endothelial cell proliferation, migration, survival, vascular permeability, and formation of new vascular networks (Pourgholami and Morris, 2008). However, angiogenic progression is not exclusively governed by growth factor signaling; extensive proteolytic remodeling of the ECM is required to permit endothelial invasion and vascular sprouting. Matrix metalloproteinases (MMPs) constitute an important proteolytic interface between ECM remodeling and tumor-associated angiogenic signaling (Kessenbrock et al., 2010). Among the MMP family, matrix metalloproteinase-9 (MMP-9; gelatinase B) has emerged as a particularly compelling therapeutic target because of its multifaceted involvement in malignant invasion, metastatic progression, microenvironment remodeling, and angiogenesis. MMP-9 is a zinc-dependent endopeptidase capable of degrading several ECM and basement-membrane components, thereby facilitating tumor-cell invasion and endothelial migration. In addition to its matrix-degrading function, MMP-9 can regulate the bioavailability of matrix-sequestered angiogenic mediators,

*Author for Correspondence: sharadwakode594@gmail.com

including VEGF, establishing a mechanistic connection between extracellular proteolysis and angiogenic activation (Vempati et al., 2014; Mondal et al., 2020). Dysregulated MMP-9 activity can facilitate tissue invasion and establish a permissive pro-angiogenic tumor microenvironment. The relevance of this protease is particularly compelling in aggressive breast cancers. MMP-9-mediated extracellular remodeling has been implicated in endothelial recruitment and neovascularization, whereas experimental suppression of MMP-9 in MDA-MB-231 TNBC models has been associated with disruption of the tumor vascular architecture. These observations support the role of MMP-9 as a molecular intersection connecting invasive tumor behavior with angiogenic competence (Shoari et al., 2026). However, the pharmacological exploitation of MMP-9 remains challenging. Earlier broad-spectrum MMP inhibitors were compromised by inadequate selectivity and mechanism-related toxicities, emphasizing the need for structurally optimized small molecules capable of achieving more effective and selective MMP-9 modulation (Fields, 2019; Mondal et al., 2020).

Within this framework, the 1,2,3-triazole nucleus represents an attractive medicinal chemistry scaffold. Its metabolic stability, hydrogen-bonding capability, strong dipolar character, and compatibility with diverse substitution patterns permit the systematic exploration of target-binding spaces. 1,2,3-Triazole-containing derivatives have demonstrated considerable potential in breast cancer drug discovery and can accommodate structural modifications to optimize potency and target selectivity (Wu et al., 2022). Incorporating this pharmacophore into a benzoylacetamide framework provides a rational platform for generating chemically diverse molecules directed toward MMP-9, while investigating their effects on angiogenic phenotypes. Accordingly, this study describes the design, synthesis, structural characterization, and biological evaluation of a new series of substituted 1,2,3-triazolyl-benzoylacetamides as MMP-9-targeted agents. The synthesized derivatives were evaluated for MMP-9 inhibitory activity, and promising candidates were selected for biological assessment in the MDA-MB-231 triple-negative breast cancer model and functional evaluation of anti-angiogenic activity in endothelial cell assays. The integration of molecular modeling, enzyme inhibition, cancer cell evaluation, and endothelial angiogenesis assays was performed to establish structure–activity relationships and identify promising triazolyl-benzoylacetamide leads capable of coupling MMP-9 inhibition with the suppression of angiogenic phenotypes.

MATERIALS AND METHODS

Rational Design and Pharmacophore Analysis

MMP-9 Protein Preparation and Binding-Site Definition

A suitable high-resolution X-ray crystal structure of human MMP-9 was retrieved from the Protein Data Bank (PDB) and prepared using the Protein Preparation Wizard in Schrödinger. Bond orders were assigned, hydrogen atoms were added, and the protonation and tautomeric states of ionizable residues were optimized at pH 7.4 ± 0.5 using PROPKA. Non-essential crystallographic water molecules were removed, whereas the catalytic Zn^{2+} and structural Ca^{2+} ions were retained. The prepared protein was subjected to restrained energy minimization using the OPLS forcefield. The MMP-9 binding site, encompassing the catalytic Zn^{2+} center and S1′ specificity pocket, was defined based on the experimentally characterized ligand-binding region. Hydrophobic, hydrogen-bond donor/acceptor, and potential metal-interacting regions within the binding cavity were identified, and a receptor grid encompassing the catalytic center and S1′ pocket was generated for subsequent molecular docking studies (Sastry et al., 2013).

Pharmacophore Development, Scaffold Selection, and Analog Design

An energy-based pharmacophore model was generated using the Phase module of Schrödinger based on the spatial and physicochemical features of the MMP-9 active site and structurally characterized MMP-9 ligands (Olsson et al., 2011). The model incorporated hydrogen-bond donor/acceptor, aromatic/hydrophobic, and metal-interacting/polar recognition features, with the hydrophobic region directed toward the S1′ specificity pocket of the target protein. Pharmacophore hypotheses were ranked using Phase scoring parameters, and the selected model guided scaffold selection and analog design (Dixon et al., 2006**)**. Accordingly, N-{4,5-dimethoxy-2-[5-(phenoxymethyl)-4H-1,2,3-triazole-4-carbonyl]phenyl}acetamide was selected as the parent scaffold, comprising an acetamide-substituted aromatic core, triazole-carbonyl polar recognition region, and phenoxymethyl hydrophobic extension. The triazole-carbonyl group is a non-hydroxamate polar recognition motif, and its interaction with the MMP-9 catalytic environment was evaluated by molecular docking. A focused library of 13 derivatives was designed through systematic modifications at R^1 and R^2. R^1 modification varied the alkyl component of the 4-alkoxy substituent to modulate the steric and hydrophobic properties, whereas R^2 substitution of the terminal phenoxy ring explored the electronic, steric, and lipophilic effects. The common acetamidobenzoyl-triazole-carbonyl-phenoxymethyl framework was retained throughout the series.

Synthesis

Fischer Esterification for Non-Basic Substrates (2a–c)

The appropriate 3-substituted-4-methoxybenzoic acid (**1a–c**) (10.0 mmol) was dissolved in absolute methanol (25 mL), and the solution was cooled to 0 °C. Concentrated sulfuric acid (H_2SO_4, 0.5 mL) was added dropwise under continuous stirring. The reaction mixture was fitted with a reflux condenser and heated at 65 °C for 8–12 h. The reaction progress was monitored by thin-layer chromatography (TLC) using *n*-hexane/ethyl acetate (7:3) as the mobile phase. After the reaction was complete, methanol was removed under reduced pressure. The residue was diluted with ice-cold water (50 mL) and extracted using ethyl acetate (3 × 30 mL). The combined organic layers were washed successively with saturated aqueous $NaHCO_3$ solution (2 × 30 mL), water (30 mL), and brine (30 mL),

dried over anhydrous Na_2SO_4, filtered, and concentrated under reduced pressure to afford the corresponding methyl ester derivatives, **2a–c**.

- Methyl 3,4-dimethoxybenzoate **(2a):** Prepared from 3,4-dimethoxybenzoic acid (**1a, 1.82 g)** was used to prepare a white solid with a yield of 92%.
- Methyl 3-ethoxy-4-methoxybenzoate **(2b):** Prepared from 3-ethoxy-4-methoxybenzoic acid (**1b**, 1.96 g**)** was used to prepare a white crystalline solid; yield: 90%.
- Methyl 3-isopropoxy-4-methoxybenzoate **(2c)**: Prepared from 3-isopropoxy-4-methoxybenzoic acid (**1c,** 2.10 g**)** was used to prepare a pale-yellow viscous oil; yield: 88%.

Esterification of the Basic Amine-Containing Substrate (2d)

3-[2-(Dimethylamino)ethoxy]-4-methoxybenzoic acid (**1d**) (2.39 g, 10.0 mmol, 1.0 equiv) was dissolved in absolute methanol (30 mL), and the solution was cooled to 0 °C in an ice bath. Thionyl chloride ($SOCl_2$, 1.5 mL, 20.0 mmol, 2.0 equiv.) was added dropwise under a nitrogen atmosphere. After the addition, the reaction mixture was stirred at room temperature for 30 min and subsequently refluxed at 65 °C for 10 h. The reaction progress was monitored by TLC using chloroform/methanol (9:1) as the mobile phase. After completion, methanol and excess thionyl chloride were removed under reduced pressure.

The resulting residue was carefully diluted with ice-cold water (40 mL), and the aqueous phase was adjusted to pH 8–9 using a saturated aqueous $NaHCO_3$ solution. The product was extracted with dichloromethane (3 × 30 mL), washed with brine, dried over anhydrous Na_2SO_4, filtered, and concentrated under reduced pressure to afford methyl 3-[2-(dimethylamino)ethoxy]-4-methoxybenzoate (**2d**) as a light brown syrup (85% yield).

Nitration of Methyl 3-Substituted-4-Methoxybenzoates: Synthesis of 3a–3d

The corresponding methyl 3-substituted-4-methoxybenzoate **2a–2d** (10.0 mmol, 1.0 equiv) was added portionwise to concentrated sulfuric acid (15 mL) under continuous stirring at 0–5 °C. A precooled nitrating mixture consisting of concentrated nitric acid (10.0 mmol, 1.0 equiv) and concentrated sulfuric acid (5 mL) was added dropwise while maintaining the reaction temperature below 5 °C. After complete addition, the reaction mixture was stirred at 0–5 °C for 30 min and subsequently allowed to reach room temperature, where stirring was continued for 2–4 h. The reaction progress was monitored by TLC using an appropriate *n*-hexane/ethyl acetate solvent system. Upon completion, the reaction mixture was slowly poured onto crushed ice with constant stirring. The resulting mixture was extracted with ethyl acetate (3 × 30 mL). The combined organic layers were washed successively with cold water, saturated aqueous $NaHCO_3$ solution, and brine, dried over anhydrous Na_2SO_4, filtered, and concentrated under reduced pressure. The crude products were purified by recrystallization or silica gel column chromatography using *n*-hexane/ethyl acetate as the eluent to obtain the corresponding 5-nitro-substituted methyl benzoate derivatives **3a–3d.**

The obtained products were as follows:

- Methyl 3,4-dimethoxy-5-nitrobenzoate (**3a**) obtained by the nitration of methyl 3,4-dimethoxybenzoate (**2a**).
- Methyl 3-ethoxy-4-methoxy-5-nitrobenzoate (**3b**) was obtained from methyl 3-ethoxy-4-methoxybenzoate (**2b**).
- Methyl 3-isopropoxy-4-methoxy-5-nitrobenzoate **(3c)** was obtained from methyl 3-isopropoxy-4-methoxybenzoate (**2c**).
- Methyl 3-[2-(dimethylamino)ethoxy]-4-methoxy-5-nitrobenzoate **(3d)** was obtained from methyl 3-[2-(dimethylamino)ethoxy]-4-methoxybenzoate (**2d**).

For amine-containing derivative **2d**, the tertiary amino group remained protonated under strongly acidic nitration conditions. Following completion of the reaction, the quenched mixture was carefully basified to approximately pH 8–9 with saturated aqueous $NaHCO_3$ solution before extraction with dichloromethane or ethyl acetate to recover the free-base form of **3d**. All isolated products were dried under vacuum and subsequently used for the next synthetic transformation after confirming their identity and purity using appropriate spectroscopic and chromatographic methods.

Reduction of Methyl Esters to Aldehydes: Synthesis of 4a–4d

The corresponding methyl 3-substituted-4-methoxy-5-nitrobenzoate derivatives **3a–3d** (10.0 mmol, 1.0 equiv) were dissolved in anhydrous toluene (40–50 mL) under a nitrogen atmosphere and cooled to **−78 °C**. A solution of diisobutylaluminium hydride (DIBAL-H, 1.0 M in toluene, 12–15 mmol, 1.2–1.5 equiv.) was added dropwise while maintaining the temperature below −70 °C. The reaction mixture was stirred at −78 °C for 1–2 h, and the reaction progress was monitored by TLC. After completion, the reaction was quenched cautiously at −78 °C by sequential addition of methanol, followed by saturated aqueous sodium potassium tartrate solution. The mixture was allowed to warm gradually to room temperature and stirred until the aluminum salts were completely decomposed. The product was extracted with ethyl acetate (3 × 30 mL), and the combined organic layers were washed with water and brine, dried over anhydrous Na_2SO_4, filtered, and concentrated under reduced pressure. The crude products were purified by silica gel column chromatography using *n*-hexane/ethyl acetate to afford the corresponding aldehydes **4a–4d**.

The resulting aldehydes were as follows:

- 3,4-Dimethoxy-5-nitrobenzaldehyde **(4a)** from ester 3a, respectively.
- 3-Ethoxy-4-methoxy-5-nitrobenzaldehyde **(4b)** from ester **3b**:
- 3-Isopropoxy-4-methoxy-5-nitrobenzaldehyde **(4c)** from ester **3c**:
- 3-[2-(Dimethylamino)ethoxy]-4-methoxy-5-nitrobenzaldehyde **(4d)** from ester **3d**.

The isolated aldehydes were dried under vacuum and used in the subsequent synthetic step after confirming their identity and purity by appropriate chromatographic and spectroscopic analyses.

Synthetic Procedure for Derivatives 6a–m

Step 1: Grignard Addition to Aldehydes 4a–d

The appropriate substituted nitrobenzaldehyde derivative **4a–d** (5.0 mmol, 1.0 equiv) was dissolved in anhydrous THF (15 mL) in a flame-dried two-necked round-bottom flask equipped with a magnetic stirrer and an inert-gas inlet. The reaction mixture was cooled to **0 °C** in an argon atmosphere. A freshly prepared THF solution of the corresponding [5-(substituted phenoxymethyl)-1,2,3-triazol-4-yl]magnesium bromide derivative **5a–f** (6.0 mmol, 1.2 equiv) was added dropwise over approximately 20 min, while the temperature was maintained at 0 °C. After complete addition, the reaction mixture was gradually warmed to room temperature and stirred for 3 h under an inert atmosphere. The reaction progress was monitored by TLC using *n*-hexane/ethyl acetate (6:4). Upon completion, the mixture was cooled to 0 °C and carefully quenched with a saturated aqueous NH_4Cl solution (20 mL). The resulting mixture was extracted using ethyl acetate (3 × 25 mL). The combined organic layers were washed successively with water (20 mL) and brine (20 mL), dried over anhydrous Na_2SO_4, filtered, and concentrated under reduced pressure to afford the corresponding secondary alcohol intermediates. The crude intermediates were used directly

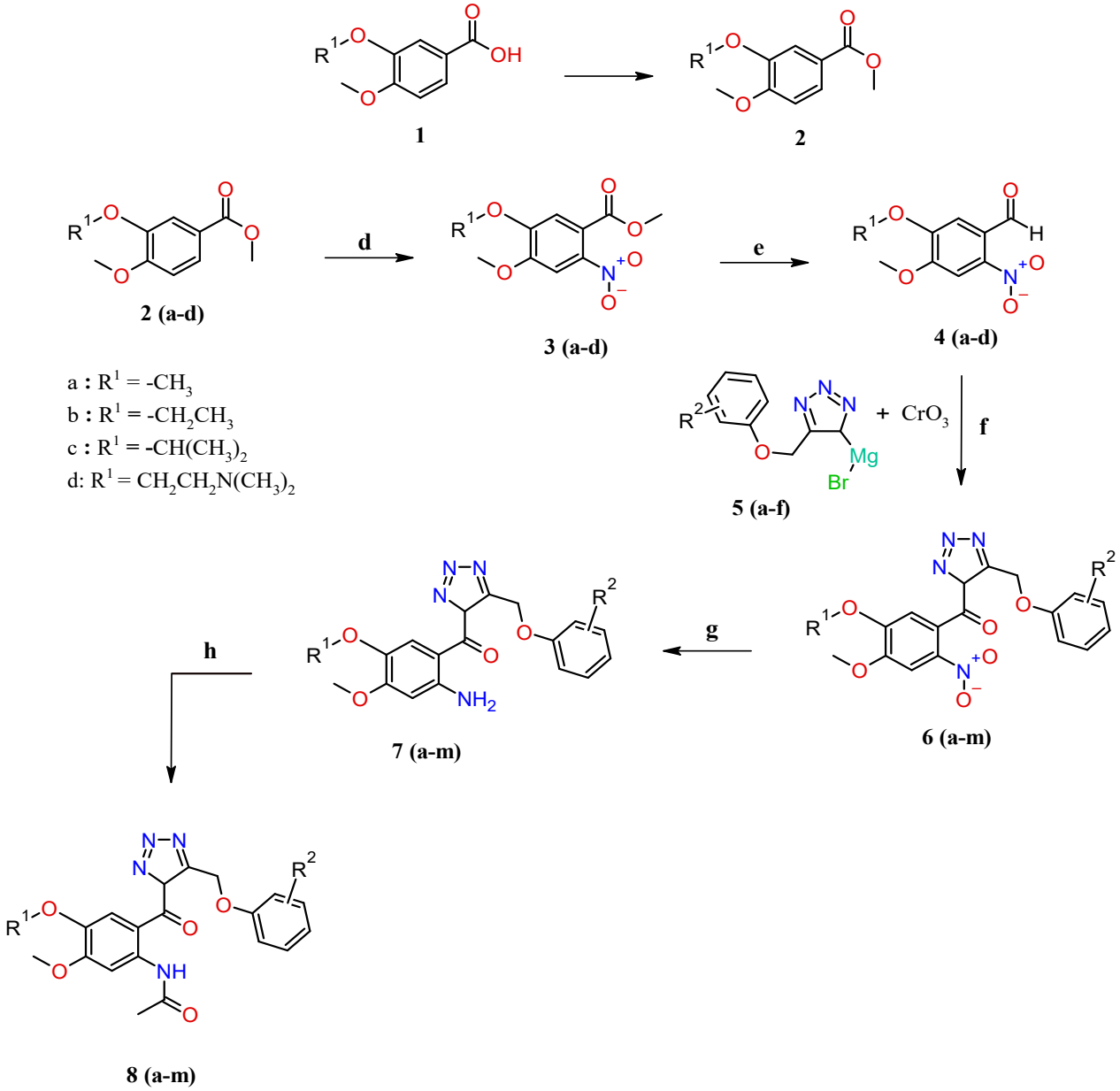

Scheme 1. General synthetic route for the target substituted 1,2,3-triazolyl-benzoylacetamide derivatives **8a–8m**. Reagents and conditions: (a) for **1a–1c**, absolute MeOH, conc. H_2SO_4, 0 °C → 65 °C, 8–12 h; (b) for **1d**, $SOCl_2$, absolute MeOH, N_2, 0 °C → rt → 65 °C, 10 h; (c) conc. HNO_3/conc. H_2SO_4, 0–5 °C → rt, 2–4 h; (d) DIBAL-H, anhydrous toluene, N_2, −78 °C, 1–2 h; (e) substituted [5-(phenoxymethyl)-1,2,3-triazol-4-yl]magnesium bromide **5a–5f**, anhydrous THF, Ar, 0 °C → rt, 3 h, followed by activated MnO_2, anhydrous DCM, rt, 6–8 h; (f) Fe (5.0 equiv), NH_4Cl, EtOH/H_2O (4:1, v/v), reflux (~80 °C), 2–4 h; (g) Ac_2O, Et_3N, dry DCM, 0 °C → rt, 1–2 h

in the subsequent oxidation step, without further purification.

Step 2: Oxidation of Secondary Alcohols to Ketones

The crude secondary alcohol intermediate obtained in step 1 was dissolved in anhydrous dichloromethane (30 mL). Activated manganese dioxide (MnO_2, 25.0 mmol, 5.0 equiv) was added in portions at room temperature, and the reaction mixture was stirred for 6–8 h. The reaction progress was monitored by TLC using *n*-hexane/ethyl acetate (1:1). After completion, the reaction mixture was filtered through a Celite pad to remove the insoluble manganese residues, and the pad was thoroughly washed with dichloromethane (3 × 15 mL). The combined filtrates were concentrated under reduced pressure, and the resulting crude products were purified by silica gel column chromatography (100–200 mesh) using a gradient of *n*-hexane/ethyl acetate as the eluent. The corresponding substituted nitrophenyl-[5-(substituted phenoxymethyl)-4H-1,2,3-triazol-4-yl]methanone derivatives 6a–m were obtained as off-white to pale-yellow solids. Alternatively, when required, the secondary alcohol intermediate was oxidized using pyridinium chlorochromate (PCC, 7.5 mmol, 1.5 equiv) in anhydrous dichloromethane at room temperature for 6–8 h, followed by filtration through Celite and chromatographic purification as described above.

Synthesis of (2-Amino-4-substituted-5-methoxyphenyl)[5-(phenoxymethyl)-4H-1,2,3-triazol-4-yl]methanone derivatives (7a–m)

The appropriate (4-substituted-5-methoxy-2-nitrophenyl)[5-(phenoxymethyl)-4H-1,2,3-triazol-4-yl]methanone derivative (6a–m) (2.0 mmol, 1.0 equiv) was dissolved in ethanol/water (4:1 v/v; 25 mL). Iron powder (Fe, 0.56 g, 10.0 mmol, 5.0 equiv) and ammonium chloride (NH_4Cl, 0.53 g, 10.0 mmol, 5.0 equiv) were added, and the reaction mixture was heated at reflux (~80 °C) for 2–4 h with constant stirring. The reaction progress was monitored by TLC using chloroform/methanol (95:5) or *n*-hexane/ethyl acetate (1:1). After complete consumption of the starting material, the hot reaction mixture was filtered through a Celite pad to remove residual iron and insoluble iron salts, and the filter cake was washed with hot EtOH (3 × 15 mL). The combined filtrates were concentrated under reduced pressure, and the resulting residue was dissolved in ethyl acetate (40 mL). The organic phase was washed successively with saturated aqueous $NaHCO_3$ solution (20 mL) and brine (20 mL), dried over anhydrous Na_2SO_4, filtered, and concentrated under reduced pressure. The crude products were purified by recrystallization from ethanol or by silica-gel column chromatography (100–200 mesh) using a DCM/MeOH gradient to afford the corresponding derivatives (**7a–m**) as yellow to light-orange solids with yields of 78–88 %.

Synthesis of N-{4-Substituted-5-methoxy-2-[5-(phenoxymethyl)-4H-1,2,3-triazole-4-carbonyl]phenyl}acetamide derivatives (8a–m)

The appropriate (2-amino-4-substituted-5-methoxyphenyl)[5-(phenoxymethyl)-4*H*-1,2,3-triazol-4-yl]methanone derivative **(7a–m)** (1.5 mmol, 1.0 equiv) was dissolved in dry dichloromethane (DCM, 15 mL), and the solution was cooled to 0 °C. Triethylamine (Et_3N, 0.31 mL, 2.25 mmol, 1.5 equiv) was added, followed by the dropwise addition of acetic anhydride (Ac_2O, 0.18 mL, 1.88 mmol, 1.25 equiv) over approximately 5 min. The reaction mixture was allowed to warm to room temperature and stirred for 1–2 h. The reaction progress was monitored by TLC using *n*-hexane/ethyl acetate (1:1) or chloroform/methanol (9:1). Upon completion, the reaction mixture was diluted with DCM (20 mL) and washed successively with 1 M HCl (15 mL), saturated aqueous $NaHCO_3$ solution (15 mL), and brine (15 mL). The organic layer was dried over anhydrous Na_2SO_4, filtered, and concentrated under reduced pressure. The crude products were purified by recrystallization from absolute ethanol or by silica-gel column chromatography (100–200 mesh) using a DCM/MeOH gradient to afford the corresponding derivatives (**8a–m**) as white to off-white crystalline solids with yields of 82–92 %.

Structural Characterization

1. *N*-{4,5-Dimethoxy-2-[5-(phenoxymethyl)-4*H*-1,2,3-triazole-4-carbonyl]phenyl}acetamide (**8a**): Yield: 76.8%; Purity: 98.2% (HPLC); MP: 168–170 °C. Molecular formula: $C_{20}H_{20}N_4O_5$; MW: 396.40 g/mol. ^{1}H NMR (500 MHz, DMSO-d_6) δ 2.148 (s, 3H), 3.759 (s, 3H), 3.819 (s, 3H), 5.179 (d, J = 12.36 Hz, 1H), 5.282 (d, J = 12.59 Hz, 1H), 6.916–6.979 (m, 2H), 7.299 (t, J = 7.55 Hz, 1H), 7.643 (s, 1H), 7.816 (s, 1H), 10.889 (s, 1H); ^{13}C NMR (125 MHz, DMSO-d_6) δ 187.74, 168.96, 163.27, 158.80, 152.86, 144.19, 136.99, 129.86, 121.63, 119.93, 115.06, 113.63, 105.61, 70.89, 65.25, 56.22, 56.09, 23.33. HRMS (ESI): *m/z* calcd for $C_{20}H_{21}N_4O_5$ $[M+H]^+$, 397.1506; found, 397.1507.

2. *N*-(2-{5-[(4-Fluorophenoxy)methyl]-4*H*-1,2,3-triazole-4-carbonyl}-4,5-dimethoxyphenyl) acetamide (**8b**): Yield: 72.5%; Purity: 97.6% (HPLC); MP: 174–176 °C. Molecular formula: $C_{20}H_{19}FN_4O_5$; MW: 414.39 g/mol. ^{1}H NMR (500 MHz, DMSO-d_6) δ 2.145 (s, 3H), 3.758 (s, 3H), 3.821 (s, 3H), 5.162 (d, J = 12.35 Hz, 1H), 5.265 (d, J = 12.55 Hz, 1H), 6.985–7.042 (m, 2H), 7.120–7.185 (m, 2H), 7.638 (s, 1H), 7.812 (s, 1H), 10.882 (s, 1H); ^{13}C NMR (125 MHz, DMSO-d_6) δ 187.70, 168.92, 163.20, 157.35 (d, JC–F = 236.2 Hz), 155.08, 152.82, 144.15, 136.95, 119.90, 116.42 (d, JC–F = 8.2 Hz), 116.10 (d, JC–F = 22.8 Hz), 113.60, 105.58, 65.80, 56.20, 56.05, 23.30. HRMS (ESI): *m/z* calcd for $C_{20}H_{20}FN_4O_5$ $[M+H]^+$, 415.1412; found, 415.1406.

3. *N*-(2-{5-[(4-Chlorophenoxy)methyl]-4*H*-1,2,3-triazole-4-carbonyl}-4,5-dimethoxyphenyl) acetamide (**8c**): Yield: 81.4%; Purity: 98.7% (HPLC); MP: 182–184 °C. Molecular formula: $C_{20}H_{19}ClN_4O_5$; MW: 430.84 g/mol. ^{1}H NMR (500 MHz, DMSO-d_6) δ 2.146 (s, 3H), 3.760 (s, 3H), 3.820 (s, 3H), 5.175 (d, J = 12.40 Hz, 1H), 5.278 (d, J = 12.60 Hz, 1H), 7.012 (d, J = 8.85 Hz, 2H), 7.345 (d, J = 8.85 Hz, 2H), 7.640 (s, 1H), 7.815 (s, 1H), 10.885 (s, 1H); ^{13}C NMR (125 MHz, DMSO-d_6) δ 187.72, 168.94, 163.25, 157.40, 152.84, 144.18, 136.98, 129.62, 125.30, 119.92, 116.85, 113.62,

105.60, 65.55, 56.21, 56.08, 23.32. HRMS (ESI): *m/z* calcd for $C_{20}H_{20}ClN_4O_5$ $[M+H]^+$, 431.1116; found, 431.1112.

4. N-(2-{5-[(4-Bromophenoxy)methyl]-4*H*-1,2,3-triazole-4-carbonyl}-4,5-dimethoxyphenyl) acetamide (**8d**): Yield: 69.7%; Purity: 96.4% (HPLC); MP: 188–190 °C. Molecular formula: $C_{20}H_{19}BrN_4O_5$; MW: 475.30 g/mol. ^{1}H NMR (500 MHz, DMSO-*d*$_6$) δ 2.147 (s, 3H), 3.761 (s, 3H), 3.822 (s, 3H), 5.178 (d, *J* = 12.38 Hz, 1H), 5.280 (d, *J* = 12.58 Hz, 1H), 6.962 (d, *J* = 8.90 Hz, 2H), 7.468 (d, *J* = 8.90 Hz, 2H), 7.642 (s, 1H), 7.816 (s, 1H), 10.888 (s, 1H); ^{13}C NMR (125 MHz, DMSO-*d*$_6$) δ 187.73, 168.95, 163.26, 157.88, 152.85, 144.19, 136.99, 132.52, 119.93, 117.38, 113.63, 113.05, 105.61, 65.48, 56.22, 56.09, 23.33. HRMS (ESI): *m/z* calcd for $C_{20}H_{20}BrN_4O_5$ $[M+H]^+$, 475.0615; found, 475.0610.

5. N-(2-{5-[(4-(Trifluoromethyl)phenoxy) methyl]-4*H*-1,2,3-triazole-4-carbonyl}-4,5-dimethoxyphenyl) acetamide (**8e**): Yield: 78.2%; Purity: 97.9% (HPLC); MP: 176–178 °C. Molecular formula: $C_{21}H_{19}F_3N_4O_5$; MW: 464.40 g/mol. ^{1}H NMR (500 MHz, DMSO-*d*$_6$) δ 2.148 (s, 3H), 3.762 (s, 3H), 3.823 (s, 3H), 5.240 (d, *J* = 12.45 Hz, 1H), 5.342 (d, *J* = 12.65 Hz, 1H), 7.185 (d, *J* = 8.50 Hz, 2H), 7.645 (s, 1H), 7.682 (d, *J* = 8.50 Hz, 2H), 7.818 (s, 1H), 10.890 (s, 1H); ^{13}C NMR (125 MHz, DMSO-*d*$_6$) δ 187.75, 168.97, 163.28, 161.22, 152.87, 144.20, 137.00, 127.22 (q, *J*C–F = 3.6 Hz), 124.62 (q, *J*C–F = 270.8 Hz), 122.15 (q, *J*C–F = 32.2 Hz), 119.94, 115.52, 113.64, 105.62, 65.40, 56.23, 56.10, 23.34. HRMS (ESI): *m/z* calcd for $C_{21}H_{20}F_3N_4O_5$ $[M+H]^+$, 465.1380; found, 465.1372.

6. N-(2-{5-[(4-Cyanophenoxy)methyl]-4*H*-1,2,3-triazole-4-carbonyl}-4,5-dimethoxyphenyl) acetamide (**8f**): Yield: 74.6%; Purity: 96.8% (HPLC); MP: 201–203 °C. Molecular formula: $C_{21}H_{19}N_5O_5$; MW: 421.41 g/mol. ^{1}H NMR (500 MHz, DMSO-*d*$_6$) δ 2.146 (s, 3H), 3.760 (s, 3H), 3.821 (s, 3H), 5.262 (d, *J* = 12.50 Hz, 1H), 5.365 (d, *J* = 12.70 Hz, 1H), 7.168 (d, *J* = 8.80 Hz, 2H), 7.641 (s, 1H), 7.802 (d, *J* = 8.80 Hz, 2H), 7.816 (s, 1H), 10.887 (s, 1H); ^{13}C NMR (125 MHz, DMSO-*d*$_6$) δ 187.73, 168.95, 163.26, 161.80, 152.85, 144.18, 136.98, 134.45, 119.92, 119.12, 116.15, 113.62, 105.60, 103.55, 65.32, 56.21, 56.08, 23.32. HRMS (ESI): *m/z* calcd for $C_{21}H_{20}N_5O_5$ $[M+H]^+$, 422.1458; found, 422.1451.

7. N-(2-{5-[(3,4-Difluorophenoxy) methyl]-4*H*-1,2,3-triazole-4-carbonyl}-4,5-dimethoxyphenyl) acetamide (**8g**): Yield: 83.1%; Purity: 98.4% (HPLC); MP: 179–181 °C. Molecular formula: $C_{20}H_{18}F_2N_4O_5$; MW: 432.38 g/mol. ^{1}H NMR (500 MHz, DMSO-*d*$_6$) δ 2.147 (s, 3H), 3.761 (s, 3H), 3.822 (s, 3H), 5.182 (d, *J* = 12.42 Hz, 1H), 5.285 (d, *J* = 12.62 Hz, 1H), 6.815–6.862 (m, 1H), 7.152–7.210 (m, 1H), 7.325–7.392 (m, 1H), 7.642 (s, 1H), 7.817 (s, 1H), 10.888 (s, 1H); ^{13}C NMR (125 MHz, DMSO-*d*$_6$) δ 187.74, 168.96, 163.27, 154.80 (dd, *J*C–F = 8.8, 2.1 Hz), 152.86, 149.82 (dd, *J*C–F = 244.5, 14.2 Hz), 144.20 (dd, *J*C–F = 238.6, 13.5 Hz), 144.19, 136.99, 119.93, 118.05 (d, *J*C–F = 18.2 Hz), 113.63, 111.22 (d, *J*C–F = 3.5 Hz), 105.61, 105.15 (d, *J*C–F = 20.5 Hz), 65.88, 56.22, 56.09, 23.33. HRMS (ESI): *m/z* calcd for $C_{20}H_{19}F_2N_4O_5$ $[M+H]^+$, 433.1318; found, 433.1311.

8. N-(2-{5-[(4-Fluorophenoxy) methyl]-4*H*-1,2,3-triazole-4-carbonyl}-4-ethoxy-5-methoxyphenyl) acetamide (**8h**): Yield: 80.5%; Purity: 97.2% (HPLC); MP: 164–166 °C. Molecular formula: $C_{21}H_{21}FN_4O_5$; MW: 428.42 g/mol. ^{1}H NMR (500 MHz, DMSO-*d*$_6$) δ 1.365 (t, *J* = 6.95 Hz, 3H), 2.146 (s, 3H), 3.818 (s, 3H), 4.082 (q, *J* = 6.95 Hz, 2H), 5.160 (d, *J* = 12.35 Hz, 1H), 5.262 (d, *J* = 12.55 Hz, 1H), 6.982–7.040 (m, 2H), 7.118–7.182 (m, 2H), 7.635 (s, 1H), 7.810 (s, 1H), 10.880 (s, 1H); ^{13}C NMR (125 MHz, DMSO-*d*$_6$) δ 187.71, 168.93, 163.22, 157.36 (d, *J*C–F = 236.2 Hz), 155.09, 152.12, 144.10, 136.92, 119.88, 116.40 (d, *J*C–F = 8.2 Hz), 116.08 (d, *J*C–F = 22.8 Hz), 114.85, 106.12, 65.82, 64.55, 56.18, 23.31, 14.82. HRMS (ESI): *m/z* calcd for $C_{21}H_{22}FN_4O_5$ $[M+H]^+$, 429.1568; found, 429.1561.

9. N-(2-{5-[(4-Chlorophenoxy) methyl]-4*H*-1,2,3-triazole-4-carbonyl}-4-ethoxy-5-methoxyphenyl) acetamide (**8i**): Yield: 71.9%; Purity: 95.9% (HPLC); MP: 171–173 °C. Molecular formula: $C_{21}H_{21}ClN_4O_5$; MW: 444.87 g/mol. ^{1}H NMR (500 MHz, DMSO-*d*$_6$) δ 1.366 (t, *J* = 6.95 Hz, 3H), 2.147 (s, 3H), 3.819 (s, 3H), 4.084 (q, *J* = 6.95 Hz, 2H), 5.172 (d, *J* = 12.38 Hz, 1H), 5.275 (d, *J* = 12.58 Hz, 1H), 7.010 (d, *J* = 8.85 Hz, 2H), 7.342 (d, *J* = 8.85 Hz, 2H), 7.638 (s, 1H), 7.812 (s, 1H), 10.883 (s, 1H); ^{13}C NMR (125 MHz, DMSO-*d*$_6$) δ 187.72, 168.94, 163.24, 157.41, 152.14, 144.12, 136.94, 129.60, 125.28, 119.90, 116.82, 114.88, 106.15, 65.52, 64.58, 56.20, 23.32, 14.84. HRMS (ESI): *m/z* calcd for $C_{21}H_{22}ClN_4O_5$ $[M+H]^+$, 445.1273; found, 445.1265.

10. N-(2-{5-[(4-(Trifluoromethyl)phenoxy)methyl]-4*H*-1,2,3-triazole-4-carbonyl}-4-ethoxy-5-methoxyphenyl) acetamide (**8j**): Yield: 77.3%; Purity: 98.0% (HPLC); MP: 183–185 °C. Molecular formula: $C_{22}H_{21}F_3N_4O_5$; MW: 478.43 g/mol. ^{1}H NMR (500 MHz, DMSO-*d*$_6$) δ 1.368 (t, *J* = 6.95 Hz, 3H), 2.149 (s, 3H), 3.821 (s, 3H), 4.086 (q, *J* = 6.95 Hz, 2H), 5.238 (d, *J* = 12.42 Hz, 1H), 5.340 (d, *J* = 12.62 Hz, 1H), 7.182 (d, *J* = 8.50 Hz, 2H), 7.641 (s, 1H), 7.680 (d, *J* = 8.50 Hz, 2H), 7.815 (s, 1H), 10.888 (s, 1H); ^{13}C NMR (125 MHz, DMSO-*d*$_6$) δ 187.75, 168.96, 163.27, 161.20, 152.16, 144.15, 136.97, 127.20 (q, *J*C–F = 3.6 Hz), 124.60 (q, *J*C–F = 270.8 Hz), 122.12 (q, *J*C–F = 32.2 Hz), 119.92, 115.50, 114.90, 106.18, 65.38, 64.60, 56.22, 23.33, 14.85. HRMS (ESI): *m/z* calcd for $C_{22}H_{22}F_3N_4O_5$ $[M+H]^+$, 477.1536; found, 477.1531.

11. N-(2-{5-[(4-Fluorophenoxy)methyl]-4*H*-1,2,3-triazole-4-carbonyl}-4-isopropoxy-5-methoxyphenyl) acetamide (**8k**): Yield: 84.2%; Purity: 96.6% (HPLC); MP: 158–160 °C. Molecular formula: $C_{22}H_{23}FN_4O_5$; MW: 442.45 g/mol. ^{1}H NMR (500 MHz, DMSO-*d*$_6$) δ 1.285 (d, *J* = 6.05 Hz, 6H), 2.145 (s, 3H), 3.815 (s, 3H), 4.622 (sept, *J* = 6.05 Hz, 1H), 5.158 (d, *J* = 12.35 Hz, 1H), 5.260 (d, *J* = 12.55 Hz, 1H), 6.980–7.038 (m, 2H), 7.115–7.180 (m, 2H), 7.632 (s, 1H), 7.808 (s, 1H), 10.878 (s, 1H); ^{13}C NMR (125 MHz, DMSO-*d*$_6$) δ 187.70, 168.92, 163.20, 157.34 (d, *J*C–F = 236.2 Hz), 155.07, 151.25, 144.05, 136.90, 119.85, 116.38

(d, *J*C–F = 8.2 Hz), 116.05 (d, *J*C–F = 22.8 Hz), 115.90, 107.25, 71.10, 65.80, 56.15, 23.30, 22.05 (2C). HRMS (ESI): *m/z* calcd for $C_{22}H_{24}FN_4O_5$ $[M+H]^+$, 443.1725; found, 443.1719.

12. N-(2-{5-[(4-Chlorophenoxy)methyl]-4*H*-1,2,3-triazole-4-carbonyl}-4-isopropoxy-5-methoxyphenyl) acetamide (**8l**): Yield: 73.8%; Purity: 95.6% (HPLC); MP: 166–168 °C. Molecular formula: $C_{22}H_{23}ClN_4O_5$; MW: 458.90 g/mol. ^{1}H NMR (500 MHz, DMSO-d_6) δ 1.286 (d, *J* = 6.05 Hz, 6H), 2.146 (s, 3H), 3.816 (s, 3H), 4.625 (sept, *J* = 6.05 Hz, 1H), 5.170 (d, *J* = 12.38 Hz, 1H), 5.272 (d, *J* = 12.58 Hz, 1H), 7.008 (d, *J* = 8.85 Hz, 2H), 7.340 (d, *J* = 8.85 Hz, 2H), 7.635 (s, 1H), 7.810 (s, 1H), 10.880 (s, 1H); ^{13}C NMR (125 MHz, DMSO-d_6) δ 187.71, 168.93, 163.22, 157.38, 151.28, 144.08, 136.92, 129.58, 125.25, 119.88, 116.80, 115.92, 107.28, 71.12, 65.50, 56.17, 23.31, 22.06 (2C). HRMS (ESI): *m/z* calcd for $C_{22}H_{24}ClN_4O_5$ $[M+H]^+$, 459.1427; found, 459.1435.

13. N-(2-{5-[(4-Fluorophenoxy)methyl]-4*H*-1,2,3-triazole-4-carbonyl}-4-[2-(dimethylamino) ethoxy]-5-methoxyphenyl) acetamide (**8m**): Yield: 79.6%; Purity: 97.4% (HPLC); MP: 151–153 °C. Molecular formula: $C_{23}H_{26}FN_5O_5$; MW: 471.49 g/mol. ^{1}H NMR (500 MHz, DMSO-d_6) δ 2.145 (s, 3H), 2.245 (s, 6H), 2.682 (t, *J* = 5.80 Hz, 2H), 3.818 (s, 3H), 4.125 (t, *J* = 5.80 Hz, 2H), 5.160 (d, *J* = 12.35 Hz, 1H), 5.262 (d, *J* = 12.55 Hz, 1H), 6.982–7.040 (m, 2H), 7.118–7.182 (m, 2H), 7.636 (s, 1H), 7.812 (s, 1H), 10.881 (s, 1H); ^{13}C NMR (125 MHz, DMSO-d_6) δ 187.71, 168.93, 163.22, 157.35 (d, *J*C–F = 236.2 Hz), 155.08, 151.85, 144.12, 136.93, 119.89, 116.41 (d, *J*C–F = 8.2 Hz), 116.09 (d, *J*C–F = 22.8 Hz), 114.22, 106.82, 67.15, 65.81, 57.85, 56.19, 45.88 (2C), 23.32. HRMS (ESI): *m/z* calcd for $C_{23}H_{27}FN_5O_5$ $[M+H]^+$, 472.1990; found, 472.1995.

Biological Evaluation

MMP-9 Enzyme Inhibition Assay and IC_{50} Determination

The inhibitory activities of compounds **8a–8m** against MMP-9 were evaluated using a recombinant human MMP-9 fluorometric assay with quenched fluorogenic peptide substrates. Test compounds were prepared as DMSO stock solutions and serially diluted with assay buffer to obtain final concentrations of 10, 20, 40, 60, 80, and 100 nM while maintaining a constant final DMSO concentration (≤1%, v/v). Recombinant human pro-MMP-9 was activated with 1 mM 4-aminophenylmercuric acetate (APMA) at 37 °C for 2 h and diluted in an assay buffer containing 50 mM Tris-HCl (pH 7.5), 150 mM NaCl, 10 mM $CaCl_2$, 5 μM $ZnCl_2$, and 0.05% Brij-35. The assay was performed in black 96-well plates at a final volume of 100 μL/well. Activated MMP-9 (5 nM final concentration) was pre-incubated with the test compounds at 37 °C for 30 min, followed by the addition of the fluorogenic substrate (10 μM final concentration) and further incubation for 30 min at 37 °C in the dark. Fluorescence was measured at the excitation/emission wavelengths specified for the selected substrate, as described by Knight et al. (1992) and Neumann et al. (2004). Vehicle-treated enzyme and enzyme-free wells served as the activity control and background blank, respectively, while a known MMP-9 inhibitor was used as the positive control. MMP-9 inhibition was calculated as [1 − (F_test/F_vehicle)] × 100, after background correction. Concentration–response curves were constructed for compounds **8a–8m**, and IC_{50} values were determined using four-parameter nonlinear regression.

MTT-Based Cell Viability Assay in MDA-MB-231 Cells

The antiproliferative activities of compounds **8a–8m** were evaluated against MDA-MB-231 triple-negative breast cancer cells using the MTT assay (Mosmann, 1983). Cells were seeded in 96-well plates at a density of 1 × 10^4 cells/well and allowed to adhere for 24 h at 37 °C in a humidified atmosphere containing 5% CO_2. The cells were subsequently treated with compounds **8a**–**8m** at final concentrations of 1, 2.5, 5, 10, 15, 20, and 25 μM for 24 h, with the final DMSO concentration maintained at 0.1% (v/v), and vehicle-treated cells served as the control. Following treatment, 20 μL of MTT solution (5 mg/mL) was added to each well and incubated for an additional 4 h at 37 °C. The medium was then removed, and the resulting formazan crystals were dissolved in 100 μL of DMSO. Absorbance was measured at 570 nm using a microplate reader, and cell viability was calculated as a percentage relative to that of the vehicle control. Concentration–response curves were generated for each compound, and IC_{50} values were determined using nonlinear regression analysis.

Morphological Analysis of MDA-MB-231 Cells

Morphological alterations induced by the selected lead compounds **8e, 8h,** and **8l** were evaluated in MDA-MB-231 cells at their respective IC_{50} concentrations after 24 h of treatment. Cells were seeded in 6-well plates at a density of 2 × 10^5 cells/well and allowed to attach for 24 h under standard culture conditions at 37 °C and 5% CO_2. The cells were then treated with **8e, 8h, 8l,** or doxorubicin at their respective IC_{50} concentrations, and vehicle-treated cells served as the control. After 24 h of exposure, the cellular morphology was examined directly under an inverted phase-contrast microscope. Representative fields were photographed at a fixed magnification, and morphological changes, including cell shrinkage, rounding, loss of adherence, membrane blebbing, reduced cell density, and detachment from the culture surface, were qualitatively compared with those in the vehicle control and doxorubicin-treated groups.

HUVEC Migration Assay

The antimigratory effect of lead compound **8h** was evaluated in human umbilical vein endothelial cells (HUVECs) using a wound-healing assay (Liang et al. (2007). HUVECs were seeded in 24-well plates at a density of 3 × 10^4 cells/well and cultured at 37 °C in a humidified atmosphere containing 5% CO_2 until a confluent monolayer was formed. A uniform wound was generated across the monolayer, and the cells were gently washed with PBS to remove detached cells. HUVECs were then treated for **8h** at its IC_{50} and 2 × IC_{50} concentrations, or with sorafenib as the reference anti-angiogenic drug, in the presence of

VEGF (10 ng/mL). Vehicle-treated cells containing 0.1% DMSO and VEGF served as angiogenic controls. The cells were incubated for 24 h, and images of the wound area were captured immediately after scratching (0 h) and 24 h later using an inverted microscope. The wound area was quantified using ImageJ software, and endothelial migration was expressed as the percentage of wound closure relative to the initial wound area. This procedure was adapted from the HUVEC migration protocol, which used VEGF-stimulated HUVECs and compound treatment at IC_{50} and 2 × IC_{50} concentrations for 24 h.

HUVEC Tube-Formation Assay

The anti-angiogenic activity of **8h** was further evaluated using a Matrigel-based HUVEC tube formation assay (Arnaoutova and Kleinman, 2010**)**. Growth factor-reduced Matrigel was thawed overnight at 4 °C, and 50 µL/well was dispensed into pre-chilled 96-well plates and allowed to polymerize at 37 °C for 30 min. HUVECs were harvested and seeded onto polymerized Matrigel at a density of approximately 2 × 10^4 cells/well in endothelial growth medium containing VEGF (10 ng/mL). The cells were treated for **8h** at its IC_{50} and 2 × IC_{50} concentrations, while sorafenib was included as the reference anti-angiogenic control and VEGF-treated vehicle wells served as the angiogenic control. After 6 h of incubation at 37 °C with 5% CO_2, representative microscopic images were captured, and tube formation was quantified using ImageJ software by measuring the total tube length, number of branch points, junctions, and/or meshes. The extent of tube formation in the treated groups was expressed relative to that in the VEGF-treated control group.

Statistical Analysis

All experimental measurements were performed in triplicate (n = 3), and the results are expressed as mean ± standard deviation (SD). Statistical comparisons among the control, reference, and treatment groups were performed using one-way analysis of variance (ANOVA) followed by Tukey's multiple-comparison post hoc test. For concentration-dependent MMP-9 inhibition and MDA-MB-231 cell viability studies, concentration–response curves were fitted using a four-parameter logistic nonlinear regression model, from which IC_{50} values were calculated. Statistical significance was set at $p < 0.05$, with significance levels represented as $^{**}p < 0.05$, $^{*}p < 0.01$, and $p < 0.001$, as applicable.

RESULTS AND DISCUSSION

Rational Design and Molecular Architecture of Non-Hydroxamate MMP-9 Inhibitors

An energy-based, structure-guided approach was employed to design non-hydroxamate MMP-9 inhibitors while minimizing dependence on the strongly chelating hydroxamate zinc-binding group. Pharmacophore modelling using the Phase module of Schrödinger identified key recognition features within the MMP-9 catalytic domain, comprising a polar/metal-interacting region proximal to the catalytic Zn^{2+} center, hydrogen-bond donor/acceptor features within the active-site cleft, and a hydrophobic vector directed toward the S1′ specificity pocket. Based on these spatial and physicochemical requirements, N-{4,5-dimethoxy-2-[5-(phenoxymethyl)-4H-1,2,3-triazole-4-carbonyl]phenyl}acetamide (**8a**) was selected as the parent scaffold for the development of the analogs (Figure 1). The scaffold was organized into distinct pharmacophoric regions to enable subsite-directed optimization (Figure 1). The 1,2,3-triazole-carbonyl core (blue) constitutes the central non-hydroxamate polar/metal-interacting motif, providing carbonyl oxygen and triazole nitrogen atoms capable of potential coordination and polar interactions within the catalytic Zn^{2+} environment. The phenoxymethyl tail (R^2) (orange) served as the principal lipophilic vector directed toward the hydrophobic S1′ pocket and provided a site for the systematic modulation of steric, electronic, and lipophilic properties. The acetamido group (purple) supplied additional hydrogen-bond donor/acceptor functionality at the active-site rim, whereas the central phenyl ring (green) provided a rigid aromatic framework that maintained the spatial alignment of the catalytic region and S1′-directed recognition elements. The 5-methoxy substituent (grey) was retained throughout the series to preserve the local steric and electronic environments of the scaffold. In contrast, the 4-alkoxy substituent (R^1) (yellow) was selected as a variable peripheral region to modulate the steric bulk, hydrophobicity, and solvent-interface interactions. Accordingly, the R^1 and terminal phenoxy R^2 substituents were systematically varied to generate compounds **8a**–**8m** while retaining the common acetamidobenzoyl–triazole-carbonyl–phenoxymethyl framework. This modular design enabled the independent optimization of the catalytic-region recognition motif and S1′-directed hydrophobic interactions, together with peripheral physicochemical tuning. Subsequent molecular docking was employed to assess whether these pharmacophoric features adopted the anticipated orientation within the MMP-9 catalytic site and to characterize the residue-level interactions underlying the binding of the analogs.

Design and Structural Diversification of the 8a–8m Series

To investigate the influence of electronic, steric, and lipophilic properties on MMP-9 recognition, the parent scaffold was systematically diversified to generate compounds **8a–8m**. Structural optimization was primarily directed toward two regions of the scaffold: modification of the alkoxy substituent on the benzoyl ring (**R^1**) and substitution of the terminal phenoxy ring (**R^2**). These positions were selected because they permitted modulation of peripheral interactions and physicochemical properties without altering the central triazole-carbonyl recognition framework. The first subset (**8a–8g**) retained the methoxy substituent at R^1 while varying R^2 from hydrogen to 4-F, 4-Cl, 4-Br, 4-CF_3, 4-CN, and 3,4-difluoro substituents. This series was designed to examine the effects of increasing electronegativity, polarizability, steric volume, and lipophilicity in the S1′-directed region. The unsubstituted derivative **8a** served as the reference scaffold, whereas compounds **8b–8d** progressively altered the size and polarizability of the para halogen substituents. Compound

8e, containing a 4-CF_3 group, introduced a substantially more lipophilic and strongly electron-withdrawing substituent, whereas **8f** incorporated a polar cyano group to examine the contribution of dipole interactions. The 3,4-difluoro analog 8 **g was** further evaluated to determine whether the distributed fluorine substitution could improve the electrostatic and hydrophobic complementarity within the S1′ region. The second level of optimization involved the modification of R^1 while retaining the selected R^2 substituent. The replacement of methoxy with ethoxy in **8h–8j** increased the hydrophobic volume of this region, whereas isopropoxy groups in **8k** and **8l** were introduced to examine the tolerance of the outer active site region toward increased steric bulk and branching. Compound **8m** incorporated a 2-(dimethylamino)ethoxy substituent, introducing a basic and potentially ionizable functionality intended to increase polarity and provide additional opportunities for interactions near the solvent-exposed region of the binding cleft.

Structure-Based Binding Characteristics and SAR Interpretation

The structure-based optimization of the **8a**–**8m** series focused on the two peripheral regions expected to influence S1′-pocket recognition and solvent-interface interactions. Modification of the terminal phenoxy ring (R^2) generated a systematic range of electronic, steric, and lipophilic properties. Relative to unsubstituted parent **8a**, para-halogenation in **8b**–**8d** progressively altered the substituent size, polarizability, and hydrophobicity, thereby probing the steric tolerance and physicochemical preferences of the S1′-directed region. The 3,4-difluoro derivative 8 **g** was used to further examine the influence of multiple compact electron-withdrawing substituents on aromatic recognition. The incorporation of CF_3 in **8e** and **8j** substantially increased both the hydrophobic surface area and electron-withdrawing character, whereas the cyano group in **8f** introduced a strongly polar substituent with comparatively limited steric demand. Collectively, these modifications established a controlled substituent gradient for assessing the electronic, steric, and hydrophobic requirements of the terminal phenoxy region of the ligands. The R^1 alkoxy substituent was independently varied to investigate the steric and physicochemical requirements for the more solvent-accessible region of the binding cleft. The extension from methoxy to ethoxy (**8h–8j**) increased the hydrophobic volume while retaining conformational flexibility, whereas isopropoxy substitution (**8k** and **8l**) introduced greater branching and steric demand, allowing the assessment of the tolerance of the peripheral binding region toward increased substituent bulk. Compound **8m**, bearing a 2-(dimethylamino)ethoxy group, incorporated an ionizable peripheral functionality designed to explore potential additional polar or electrostatic interactions, while simultaneously modifying the overall physicochemical profile of the scaffold. Thus, the **8a**–**8m** series retained the common non-hydroxamate triazole-carbonyl recognition framework while systematically varying R^1 and R^2 to probe the contributions of steric volume, electronic character, hydrophobicity, polarizability, and ionizable functionality to MMP-9 recognition. This systematic substitution strategy provided a rational structural framework for correlating molecular architecture with the subsequent docking behavior, MMP-9 inhibitory potency, antiproliferative activity, and anti-angiogenic effects of the synthesized analogs.

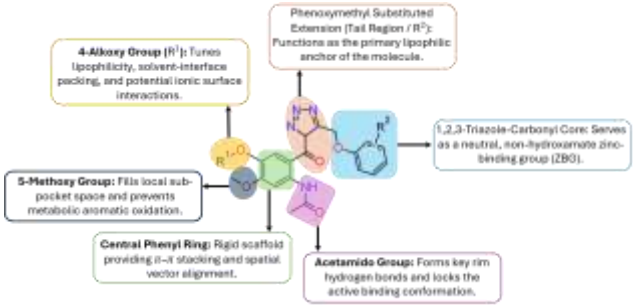

Figure 1. Structure-guided molecular architecture of the substituted 1,2,3-triazolyl-benzoylacetamide scaffold designed for MMP-9 inhibition, highlighting the 1,2,3-triazole-carbonyl polar/metal-interacting core (blue), S1′-directed phenoxymethyl R^2 region (orange), acetamido functionality (purple), central aromatic scaffold (green), conserved 5-methoxy group (grey), and variable 4-alkoxy R^1 region (yellow)

Chemistry

The synthetic strategy employed for the preparation of the target substituted 1,2,3-triazolyl-benzoylacetamide derivatives **8a–8m** is shown in Scheme 1. The route was designed to permit systematic and largely independent modification of the R^1 substituent on the benzoyl ring and the R^2 substituent on the terminal phenoxy moiety while maintaining the common acetamidobenzoyl–triazole-carbonyl pharmacophoric framework. The overall sequence involved the esterification of substituted benzoic acids, regioselective aromatic nitration, controlled reduction of the ester functionality to the corresponding aldehyde, carbon–carbon bond formation with substituted phenoxymethyl-1,2,3-triazole-derived organomagnesium intermediates, oxidation to the corresponding ketones, reduction of the aromatic nitro group, and final N-acetylation to furnish compounds 8a–8m. Initially, the appropriately substituted benzoic acids **1a–1c** were converted into their corresponding methyl esters **2a–2c** by conventional Fischer esterification using absolute methanol and concentrated H_2SO_4 under reflux at 65 °C for 8–12 h, affording the ester intermediates in 88–92% yields, respectively. Because the 2-(dimethylamino)ethoxy-substituted precursor contained a basic tertiary amine, acid **1d** was esterified under modified conditions using $SOCl_2$ in absolute methanol under nitrogen, followed by reflux at 65 °C for 10 h to provide ester 2d in an 85% yield. The resulting methyl benzoates **2a–2d** were subjected to regioselective electrophilic nitration using concentrated HNO_3/H_2SO_4. The reaction was initiated at 0–5 °C to control the exothermic process and subsequently allowed to proceed at room temperature for 2–4 h, affording the corresponding nitro esters 3a–3d in good yields. For the

tertiary amine-containing derivative, basification of the reaction mixture to approximately pH 8–9 before extraction enabled the recovery of the product in its free-base form. The ester functionality of intermediates **3a–3d** was subsequently converted to the corresponding aldehyde, while retaining the nitro substituent required for later transformation to the acetamido functionality. Controlled reduction with DIBAL-H (1.2–1.5 equiv) in anhydrous toluene was performed under nitrogen at −78 °C for 1–2 h. Careful low-temperature addition minimized over-reduction and furnished substituted nitrobenzaldehydes **4a–4d** after controlled quenching and purification. These aldehyde intermediates served as key electrophilic partners for the introduction of the triazole-containing pharmacophoric region.

The central aryl-carbonyl-1,2,3-triazole linkage was constructed via a two-step addition–oxidation sequence. The appropriate nitrobenzaldehyde **4a–4d** was reacted with the corresponding [5-(substituted phenoxymethyl)-1,2,3-triazol-4-yl]magnesium bromide **5a–5f** in anhydrous THF under an inert atmosphere. The organomagnesium reagent was added at 0 °C, after which the reaction mixture was gradually warmed to room temperature and stirred for approximately 3 h. Nucleophilic addition to the aldehyde generates the corresponding secondary alcohol intermediates, which are subsequently oxidized with activated MnO_2 in anhydrous DCM at room temperature for 6–8 h. Where required, PCC in anhydrous DCM was used as an alternative oxidizing reagent. This transformation afforded substituted nitrophenyl-[5-(substituted phenoxymethyl)-1,2,3-triazol-4-yl]methanone derivatives **6a–6m** and simultaneously established the central triazole-carbonyl recognition motif and the structurally variable R^2 phenoxymethyl region. The aromatic nitro groups of intermediates 6a–6m were then selectively reduced using Fe/NH_4Cl in $EtOH/H_2O$ (4:1, v/v) under reflux at approximately 80 °C for 2–4 h. These conditions furnished the corresponding aniline derivatives **7a–7m** in 78–88% yields without disrupting the triazole-carbonyl framework of the starting materials. Following purification, the resulting amino intermediates were subjected to final N-acetylation using Ac_2O (1.25 equiv) and Et_3N (1.5 equiv) in dry DCM, initially at 0 °C, and subsequently at room temperature for 1–2 h. Purification by recrystallization from absolute ethanol or silica gel chromatography afforded the desired acetamide derivatives **8a–8m** as white to off-white crystalline products. The synthetic route provided the intended structural diversity at both peripheral modification sites while preserving a common molecular framework. Compounds **8a–8g** retained the dimethoxy benzoyl region while varying the terminal phenoxy R^2 substituent through H, 4-F, 4-Cl, 4-Br, 4-CF_3, 4-CN, and 3,4-di-F. Further diversification of the benzoyl ring R^1 region generated ethoxy derivatives **8h–8j**, isopropoxy derivatives **8k–8l**, and 2-(dimethylamino)ethoxy derivative 8m. Thus, the developed sequence enabled systematic modulation of the electronic characteristics, steric volume, hydrophobicity, and peripheral ionizable functionality, providing a chemically coherent analog series suitable for subsequent molecular docking, MMP-9 inhibition, and structure–activity relationship studies.

Structural characterization of the final compounds supported the successful formation of the proposed target structures. The ^1H NMR spectra showed characteristic resonances attributable to the acetamide methyl group at approximately δ 2.14–2.15 ppm, methoxy functionality at approximately δ 3.75–3.82 ppm, diastereotopic phenoxymethyl protons predominantly in the δ 5.15–5.37 ppm region, aromatic/triazole-associated signals within the expected downfield region, and a characteristic acetamide NH resonance near δ 10.88 ppm. The ^{13}C NMR spectra consistently exhibited resonances for the ketonic carbonyl at approximately δ 187.7 ppm and the acetamide carbonyl at approximately δ 168.9 ppm, supporting the incorporation of the characteristic triazole-carbonyl and acetamide functionalities. Substituent-specific resonances further supported structural diversification; for example, fluorinated derivatives displayed characteristic carbon–fluorine coupling patterns, whereas ethoxy, isopropoxy, and dimethylaminoethoxy derivatives exhibited the corresponding aliphatic carbon resonances. The representative spectroscopic assignments reported for **8a–8m** are consistent with these structural features. High-resolution mass spectrometric analysis further corroborated the molecular compositions of the synthesized derivatives, with experimentally observed protonated molecular ions showing close agreement with the calculated [M + H] + values. For example, parent compound **8a** displayed an HRMS ion at *m/z 397.1507,* compared with the calculated value of 397.1506, while the 4-fluoro derivative **8b** showed *m/z 415.1406,* compared with the calculated 415.1412. Similarly, the final dimethylaminoethoxy derivative **8m** exhibited an experimental $[M+H]^+$ value of 472.1995, which closely corresponded to the calculated value of 472.1990. Together with the HPLC purities, melting-point characteristics, and NMR data, these findings support the successful synthesis and structural assignment of the **8a–8m** series.

Biological Evaluation

MMP-9 Inhibitory and Antiproliferative Activities of Compounds 8a–8m

The synthesized 1,2,3-triazolyl-benzoylacetamide derivatives **8a–8m** were evaluated for their direct MMP-9 inhibitory and antiproliferative activities against MDA-MB-231 triple-negative breast cancer cells. As summarized in Table 1, the compounds displayed distinct differences in potency across the series, with MMP-9 IC_{50} values ranging from 20.4 to 88.6 nM and MDA-MB-231 IC_{50} values ranging from 5.2 to 22.7 μM. Notably, the relative activity observed in the biochemical MMP-9 assay was broadly reflected in the cellular assay, supporting the relationship between structural modification, MMP-9 inhibitory potency, and antiproliferative activity. In the MMP-9 inhibition assay, **8h** emerged as the most potent derivative, with an IC_{50} of 20.4 ± 0.9 nM, followed by **8e** (26.3 ± 1.2 nM) and **8l** (29.6 ± 1.3 nM). These compounds exhibited activity comparable to that of the reference MMP inhibitor

NNGH (14.7 ± 1.1 nM). Compounds **8m, 8k,** and **8f** exhibited intermediate inhibitory activity, with IC_{50} values of 35.1 ± 1.5, 38.2 ± 1.6, and 41.7 ± 1.8 nM, respectively. In contrast, derivatives 8a–8d, 8 **g, 8i,** and **8j** were comparatively less potent, with IC_{50} values ranging from 60.9–88.6 nM. The concentration-dependent profiles of representative lead compounds **8e, 8h,** and **8l** are shown in Figure 2a, demonstrating the progressive enhancement of MMP-9 inhibition over the tested concentration range.

Among these derivatives, **8h** consistently exhibited the greatest inhibition, supporting its identification as the principal lead of the series. The observed differences in MMP-9 inhibitory potency also provided preliminary structure–activity relationship (SAR) information. Within the methoxy-substituted series, the introduction of a 4-CF_3 group in **8e** markedly enhanced the activity relative to the unsubstituted parent **8a** and the corresponding 4-F, 4-Cl, 4-Br, and 3,4-difluoro derivatives. The activity of **8h**, bearing an ethoxy R^1 group and 4-F substitution on the terminal phenoxy ring, indicated that a modest extension of the alkoxy substituent in combination with para-fluoro substitution was particularly favorable for MMP-9 inhibition. Interestingly, **8l**, which incorporates an isopropoxy group and 4-Cl substitution, also exhibited strong activity, suggesting that an increased hydrophobic bulk at R^1 could be accommodated when combined with an appropriate terminal phenoxy substituent. Conversely, the substantially weaker activities of **8i** and **8j** indicated that the beneficial effect of R^1 enlargement was strongly dependent on the accompanying R^2 substitution rather than being solely attributable to increased lipophilicity. Overall, these findings support the contribution of both R^1 and R^2 substituents to the productive recognition of the MMP-9 catalytic environment. The antiproliferative activity of the compounds against MDA-MB-231 cells showed a similar trend (Table 1 and Figure 2b). Compound **8h** exhibited the strongest cellular activity, with an IC_{50} of 5.2 ± 0.3 µM, followed by **8e** (6.7 ± 0.4 µM) and **8l** (7.2 ± 0.4 µM), respectively. Compounds **8m, 8k,** and **8f** displayed intermediate effects, with IC_{50} values of 8.1 ± 0.5, 9.1 ± 0.5, and 10.2 ± 0.6 µM. The remaining derivatives were less active, with IC_{50} values between 12.8 and 22.7 µM. Doxorubicin, used as a reference cytotoxic agent, showed an IC_{50} of 2.3 ± 1.9 µM. As illustrated in Figure 2b, increasing concentrations of **8e, 8h,** and **8l** progressively reduced MDA-MB-231 cell viability, with **8h** producing the greatest reduction among all the synthesized compounds. In summary, the biochemical and cellular findings identified **8h, 8e,** and **8l** as the principal active derivatives, with **8h** exhibiting the most favorable combined profile of MMP-9 inhibition and MDA-MB-231 antiproliferative activity. The parallel ranking observed across the two assays suggests that structural features favoring MMP-9 recognition are also associated with enhanced cellular activity. Nevertheless, because MTT reduction represents overall cellular metabolic viability rather than a target-specific response, the antiproliferative effects cannot be attributed exclusively to MMP-9 inhibition. Accordingly, **8h, 8e, and 8l** were selected as lead compounds for subsequent cellular MMP-9, migration/invasion, and anti-angiogenic investigations to establish the functional relevance of their biochemical MMP-9 inhibitory activities.

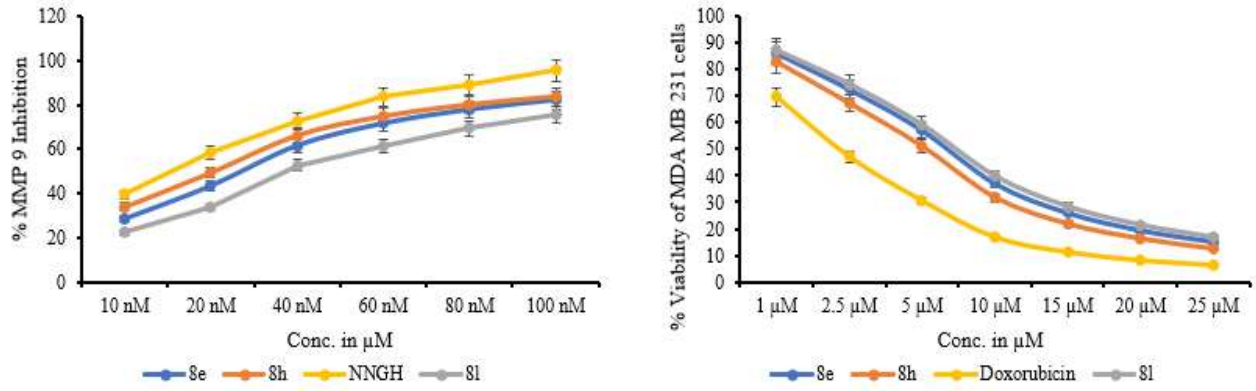

(a) (b)

Figure 2. Concentration-dependent biological activity of selected lead compounds **8e, 8h, and 8l**: **(a)** inhibition of recombinant human MMP-9 and **(b)** reduction in MDA-MB-231 cell viability. Data are presented as mean ± SD (n = 3)

Table 1. Antiproliferative and MMP-9 Inhibitory effects of **8a–8m** against MDAMB-231 Cells

Compound	R^1 at 4-OR^1	R^2 on terminal phenoxy ring	IC_{50} of MMP-09 Inhibition (nM)	IC_{50} against MDAMB-231 cells (μM)
8a	CH_3	H	88.6 ± 3.4	22.7 ± 1.2
8b	CH_3	4-F	77.1 ± 2.9	18.6 ± 0.9
8c	CH_3	4-Cl	83.7 ± 3.1	20.5 ± 1.1
8d	CH_3	4-Br	71.2 ± 2.7	16.3 ± 0.8
8e	CH_3	4-CF_3	26.3 ± 1.2	6.7 ± 0.4
8f	CH_3	4-CN	41.7 ± 1.8	10.2 ± 0.6
8g	CH_3	3,4-diF	65.4 ± 2.5	14.6 ± 0.7
8h	CH_2CH_3	4-F	20.4 ± 0.9	5.2 ± 0.3
8i	CH_2CH_3	4-Cl	74.8 ± 2.8	17.5 ± 0.9
8j	CH_2CH_3	4-CF_3	60.9 ± 2.3	12.8 ± 0.7
8k	$CH(CH_3)_2$	4-F	38.2 ± 1.6	9.1 ± 0.5
8l	$CH(CH_3)_2$	4-Cl	29.6 ± 1.3	7.2 ± 0.4
8m	$(CH_2)_2N(CH_3)_2$	4-F	35.1 ± 1.5	8.1 ± 0.5
NNGH	-	-	14.7 ± 1.1	-
DOXO	-	-		2.3 ± 1.9

Table 2. Effect of compound 8h on VEGF-induced HUVEC migration

Treatment	Concentration	Wound closure at 0 h (%)	Wound closure at 24 h (%)	Inhibition of migration (%)
Control (without VEGF)	—	0.0 ± 0.0	34.6 ± 2.8	—
VEGF control	10 ng/mL	0.0 ± 0.0	86.4 ± 3.5	—
8h (IC_{50})	5.2 μM	0.0 ± 0.0	43.8 ± 2.7	49.3 ± 3.1
8h (2×IC_{50})	10.4 μM	0.0 ± 0.0	25.7 ± 2.2	70.3 ± 2.8
Sorafenib	5 μM	0.0 ± 0.0	21.9 ± 1.9	74.7 ± 2.5

Structure–Activity Relationship of Compounds 8a–8m

Structure–activity relationship (SAR) analysis of compounds **8a**–**8m** revealed that modifications at both the R^1 alkoxy region and R^2 terminal phenoxy ring markedly influenced MMP-9 inhibition and antiproliferative activity against MDA-MB-231 cells. Overall, the cellular activity broadly followed the MMP-9 inhibitory profile, with **8h**, **8e**, and **8l** being the most active derivatives. Compound **8h** exhibited the highest potency, with IC_{50} values of 20.4 ± 0.9 nM against MMP-9 and 5.2 ± 0.3 μM against MDA-MB-231 cells, followed by **8e** (26.3 ± 1.2 nM; 6.7 ± 0.4 μM) and **8l** (29.6 ± 1.3 nM; 7.2 ± 0.4 μM). Within the $R^1 = CH_3$ series (**8a**–**8g**), the unsubstituted phenoxy derivative **8a** exhibited the weakest activity (88.6 ± 3.4 nM; 22.7 ± 1.2 μM). Para-halogen substitution produced variable improvements, whereas the introduction of 4-CF_3 in **8e** resulted in a pronounced enhancement of both MMP-9 inhibition and cellular activity. The 4-CN derivative **8f** showed intermediate potency, whereas 3,4-difluoro substitution in 8 **g** only moderately improved potency. These findings indicate that the terminal phenoxy substituent requires an appropriate combination of electronic characteristics, lipophilicity, and steric volume rather than electron withdrawal alone. The modification of R^1 further demonstrated a strong dependence on the accompanying R^2 substituent. Within the 4-F series, replacing methyl in **8b** with ethyl in **8h** markedly enhanced the activity, whereas further enlargement to isopropyl (**8k**) or introduction of a 2-(dimethylamino)ethyl group (**8m**) produced intermediate potency. Thus, the ethoxy/4-F combination at **8h** appeared optimal. In contrast, among the 4-Cl derivatives, the branched isopropyl analog **8l** was substantially more active than the methyl (**8c**) and ethyl (**8i**) analogs, suggesting the favorable accommodation of an increased R^1 hydrophobic bulk in combination with 4-Cl substitution. Conversely, although 4-CF_3 was highly favorable for the methyl derivative 8e, the introduction of an ethyl group at R^1 in **8j reduced the** activity, indicating that simultaneous increases in steric and hydrophobic volumes at both substitution sites were unfavorable.

Importantly, the biochemical and cellular activity profiles showed consistent relationships. The strongest MMP-9 inhibitors, **8h**, **8e**, and **8l**, were also the most active derivatives against MDA-MB-231 cells, whereas **8m**, **8k**, and **8f** exhibited intermediate activity, and the remaining analogs were comparatively weaker. Collectively, the SAR identified ethoxy/4-F (**8h**), methoxy/4-CF_3 (**8e**), and isopropoxy/4-Cl (**8l**) as the most favorable substitution patterns. Among these, **8h** demonstrated the optimal overall activity profile and, together with **8e** and **8l**, was prioritized for subsequent mechanistic and anti-angiogenic evaluation.

Morphological Alterations in MDA-MB-231 Cells

Phase-contrast microscopic examination revealed marked morphological alterations in MDA-MB-231 cells following 24 h of exposure to the selected lead compounds **8e, 8h,** and **8l** at their respective IC_{50} concentrations (Figure 3). Vehicle-treated control cells exhibited characteristic adherent, elongated/spindle-shaped morphology, with relatively uniform cellular distribution and high cell density. In contrast, treatment with the synthesized

Table 3. Effect of compound 8h on VEGF-induced HUVEC tube formation

Treatment	Concentration	Total tube length (% of VEGF control)	Branch points (% of VEGF control)	Junctions (% of VEGF control)	Inhibition of tube formation (%)
Control (without VEGF)	—	46.8 ± 3.2	42.5 ± 3.0	44.1 ± 3.1	—
VEGF control	10 ng/mL	100.0 ± 4.1	100.0 ± 4.5	100.0 ± 4.2	—
8h (IC_{50})	5.2 μM	54.7 ± 3.3	51.8 ± 3.1	53.6 ± 3.2	45.3 ± 3.3
8h (2×IC_{50})	10.4 μM	31.2 ± 2.5	27.6 ± 2.3	29.4 ± 2.4	68.8 ± 2.5
Sorafenib	5 μM	25.8 ± 2.2	22.4 ± 2.0	23.7 ± 2.1	74.2 ± 2.2

derivatives resulted in evident changes in cellular architecture, including cell shrinkage, rounding, reduced spreading, loss of adherence, and decreased cell density. Among the tested derivatives, **8h (5.2 μM)** induced the most pronounced morphological alterations, characterized by extensive cell rounding, shrinkage, membrane blebbing, and detachment from the culture surface. Compound **8e** (6.7 μM) similarly caused a substantial loss of normal spindle-shaped morphology, accompanied by reduced adherence and cell density. Treatment with **8l** (7.2 μM) resulted in appreciable cell rounding and shrinkage, with moderate loss of adherence. These morphological effects were consistent with the relative antiproliferative potencies observed in the MTT assay, in which **8h** showed the lowest IC_{50} among the synthesized derivatives, followed by **8e** and **8l**. Doxorubicin (2.3 μM) produced extensive rounding, blebbing, detachment, and a pronounced reduction in adherent cell density and served as the reference cytotoxic treatment. Collectively, the microscopic observations supported the MTT-based findings and demonstrated that the lead compounds induced substantial alterations in MDA-MB-231 cell morphology after 24 h of exposure. The comparatively pronounced effect of **8h** further supports its superior cellular activity within the selected lead series.

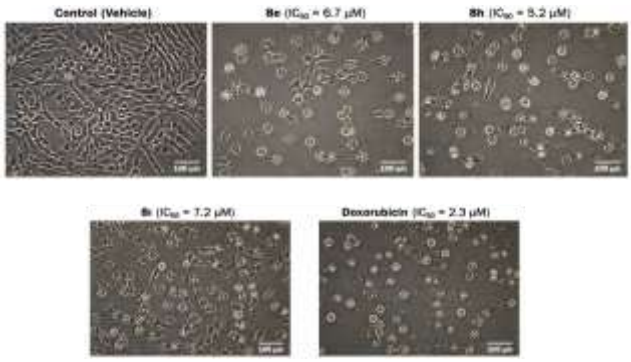

Figure 3. Morphological alterations in MDA-MB-231 cells following treatment with the selected lead compounds. Representative phase-contrast micrographs of MDA-MB-231 cells treated for 24 h with vehicle control, 8e 8h, and **8l** or doxorubicin at their respective IC_{50} concentrations.

Effect of Compound 8h on HUVEC Migration

The antimigratory activity of lead compound **8h** was evaluated in VEGF-stimulated HUVECs using a wound-healing assay. As shown in Figure 4a, VEGF stimulation markedly promoted endothelial cell migration, resulting in substantial closure of the scratched area after 24 h of treatment. Quantitative analysis (Figure 4b) showed 86.4 ± 3.5% wound closure in the VEGF-treated control compared with 34.6 ± 2.8% in the unstimulated control, confirming the pro-migratory effect of VEGF on HaCaT cells. Treatment for **8h** significantly suppressed VEGF-induced HUVEC migration in a concentration-dependent manner. At its IC_{50} concentration (5.2 μM), **8h** reduced wound closure to 43.8 ± 2.7%, corresponding to approximately 49.3% inhibition of VEGF-induced migration. Increasing the concentration to 2×IC_{50} (10.4 μM) further reduced wound closure to 25.7 ± 2.2%, representing approximately 70.3% of inhibition. The reference anti-angiogenic agent sorafenib (5 μM) produced the strongest response, limiting wound closure to 21.9 ± 1.9. The inhibitory effects of both concentrations of **8h** and sorafenib were significant compared to those of the VEGF control ($p < 0.001$). Microscopic observations were consistent with the quantitative findings, showing progressively wider residual wound areas following treatment with increasing concentrations of **8h** (Figure 4a). Notably, the effect observed at 10.4 μM approached that of sorafenib, indicating a substantial suppression of endothelial motility. As endothelial cell migration is a critical component of angiogenic sprouting and neovascularization, these findings provide functional evidence for the anti-angiogenic potential of **8h**. In addition to its potent MMP-9 inhibitory activity (IC_{50} = 20.4 ± 0.9 nM), the inhibition of VEGF-stimulated endothelial migration supports further evaluation of **8h** as the lead derivative for targeting MMP-9-associated angiogenic processes.

Effect of Compound 8h on VEGF-Induced HUVEC Tube Formation

The anti-angiogenic potential of lead compound **8h** was further evaluated using a VEGF-induced HUVEC tube-formation assay. As summarized in Table 3 and illustrated in Figure 5, VEGF stimulation induced the formation of a well-organized and highly interconnected capillary-like network, which was normalized to 100% of tube formation. In contrast, unstimulated control cells exhibited substantially reduced network formation, with total tube length, branch points, and junctions of 46.8 ± 3.2%, 42.5 ± 3.0%, and 44.1 ± 3.1%, respectively, confirming the pro-angiogenic response to VEGF under these experimental conditions. Treatment for **8h** markedly suppressed VEGF-induced endothelial network formation in a concentration-

dependent manner (Table 3; Figure 5). At its IC_{50} concentration (5.2 µM), **8h reduced the** total tube length to 54.7 ± 3.3% of the VEGF control, accompanied by reductions in branch points (51.8 ± 3.1%) and junctions (53.6 ± 3.2%), corresponding to 45.3% inhibition of tube formation. A more pronounced response was observed at $2\times IC_{50}$ (10.4 µM), where the total tube length decreased to 31.2 ± 2.5%, while branch points and junctions were reduced to 27.6 ± 2.3% and 29.4 ± 2.4%, respectively, resulting in 68.8% inhibition of VEGF-induced tube formation. The reference anti-angiogenic agent sorafenib (5 µM) produced the greatest disruption of endothelial network organization, reducing the total tube length, branch points, and junctions to 25.8 ± 2.2%, 22.4 ± 2.0%, and 23.7 ± 2.1%, respectively, corresponding to 74.2 ± 2.2% inhibition (Table 3; Figure 5). Notably, the inhibitory response at **8h** and 10.4 µM approached that of sorafenib, indicating substantial suppression of VEGF-driven endothelial network formation. Collectively, the concentration-dependent reductions in tube length, branching, and junction formation demonstrated that 8h treatment impaired multiple structural events required for capillary-like network development. These findings, along with its potent MMP-9 inhibitory activity (IC_{50} = 20.4 ± 0.9 nM) and suppression of VEGF-induced HUVEC migration, further support the anti-angiogenic potential of **8h**.

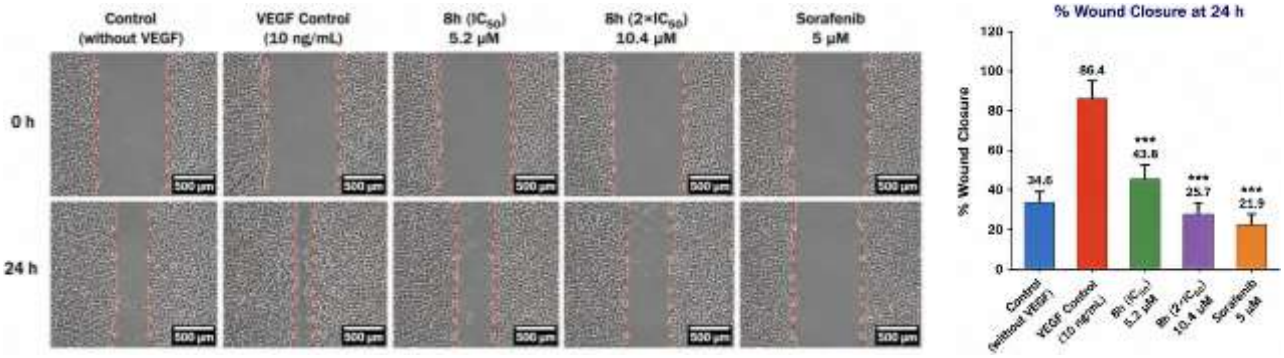

(a) (b)

Figure 4. Effect of compound 8h on VEGF-induced HUVEC migration. **(a)** Representative phase-contrast images of HUVEC wound closure at 0 and 24 h under control (without VEGF), VEGF control (10 ng/mL), **8h** at IC_{50} (5.2 µM)**, 8h** at $2\times IC_{50}$ (10.4 µM)**,** and sorafenib (5 µM) treatment conditions. The red dashed lines indicate the boundary of the wound. Scale bar = 500 µm. **(b)** Quantitative analysis of wound closure after 24 h. VEGF markedly enhanced endothelial cell migration, whereas **8h** significantly inhibited wound closure in a concentration-dependent manner, with the $2\times IC_{50}$ treatment approaching the inhibitory effect of sorafenib. Data are expressed as mean ± SD (n = 3)**.** $^{**}p < 0.001$ versus VEGF control

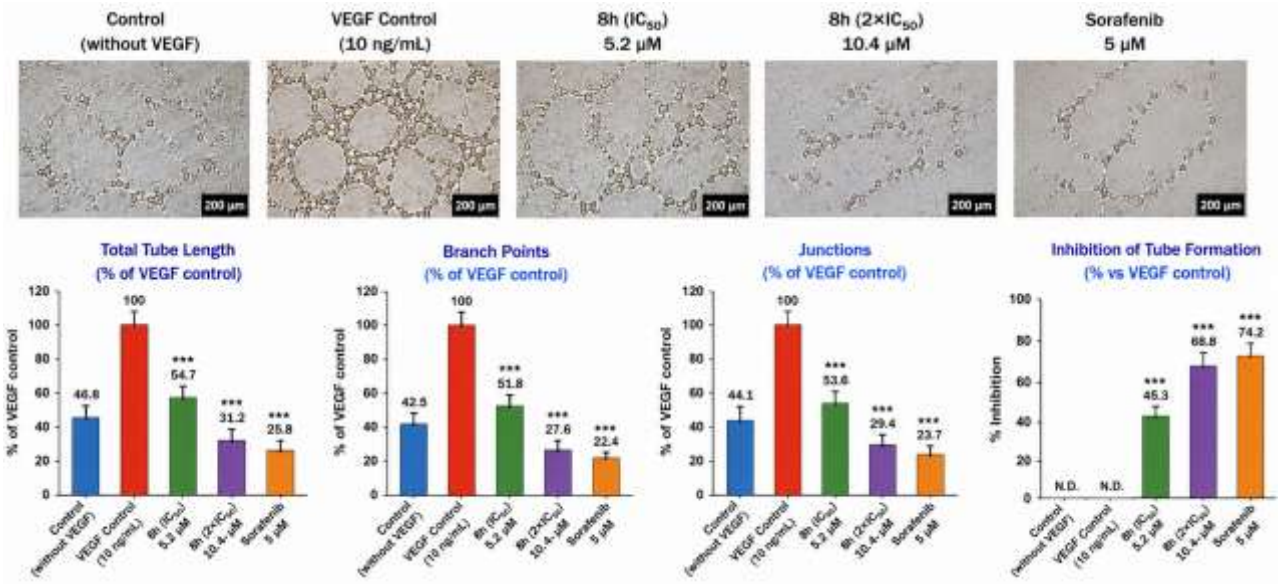

Figure 5. Effect of compound **8h** on VEGF-induced HUVEC tube formation. Representative microscopic images showing capillary-like network formation in HUVECs under control (without VEGF), VEGF-stimulated control (10 ng/mL), **8h** at IC_{50} (5.2 µM), **8h** at $2\times IC_{50}$ (10.4 µM), and sorafenib (5 µM) treatment conditions. Quantitative analysis of total tube length, branch points, junctions, and percentage inhibition of tube formation demonstrated a concentration-dependent suppression of VEGF-induced endothelial network formation after **8h**, with the effect at $2\times IC_{50}$ approaching that of sorafenib. Tube formation parameters were normalized to the VEGF control (100%). Data are expressed as mean ± SD (n = 3). $^{**}p < 0.001$ versus VEGF control. Scale bar = 200 µm

However, because tube formation represents a functional angiogenic phenotype rather than a direct measure of MMP-9 activity, these findings establish anti-angiogenic efficacy but do not, by themselves, demonstrate that the observed effect is exclusively mediated through MMP-9 inhibition.

CONCLUSION

The present study established a rational framework for the discovery and optimization of substituted 1,2,3-triazolyl-benzoylacetamides as non-hydroxamate MMP-9 inhibitors with anti-angiogenic potential in triple-negative breast cancer. Structure-guided pharmacophore modelling enabled the identification of the key molecular features required for the productive recognition of the MMP-9 catalytic environment and provided the basis for designing a scaffold that integrates a triazole-carbonyl polar recognition motif with an S1′-directed phenoxymethyl hydrophobic region. Systematic diversification of peripheral substituents generated a focused analog series suitable for defining the steric, electronic, and hydrophobic requirements governing biological activity. The developed synthetic strategy provided efficient access to the designed compounds, allowing independent modification of the principal structural regions. Biological evaluation revealed a coherent structure–activity relationship, demonstrating that appropriate combinations of substitutions at the benzoyl and terminal phenoxy regions were critical for enhancing the MMP-9 inhibitory and cellular activities. Among the synthesized derivatives, **8h** emerged as the principal lead, whereas **8e** and **8l** also displayed favorable activity profiles, collectively defining the structural features that may guide further scaffold optimization. Importantly, the biological effects of the lead compound extend beyond direct enzyme inhibition. Compound **8h** suppressed the viability of MDA-MB-231 cells and induced marked morphological alterations consistent with impaired cellular integrity. Furthermore, its ability to inhibit VEGF-stimulated HUVEC migration and disrupt capillary-like tube formation provides functional evidence of anti-angiogenic activity. The convergence of MMP-9 inhibition, antiproliferative activity, and suppression of endothelial angiogenic responses supports the pharmacological relevance of this scaffold in aggressive breast cancer. Overall, the findings identify the 1,2,3-triazolyl-benzoylacetamide framework as a promising non-hydroxamate chemotype for MMP-9-directed anti-angiogenic drug discovery. The lead compound **8h** is a suitable candidate for subsequent investigations of target selectivity, mechanism, pharmacokinetics, safety, and *in vivo* efficacy, aimed at establishing its potential for further preclinical development.

Acknowledgments

We acknowledge the ACITE-National Doctoral Fellowship, New Delhi, India, for granting a Senior Research Fellowship (SRF). The authors thank the Delhi Institute of Pharmaceutical Science and Research (DIPSAR), Delhi Pharmaceutical Science Research University, New Delhi for providing the necessary facilities.

Author Credits

Shaik Khasimbi: Conceptualization, Investigation, Work execution, Writing-original draft, Writing- Editing. Sharad Wakode**:** Supervision, guidance, Writing- Review.

REFERENCES

1. Han, M. I., Atalay, P., & Satir-Basaran, G. (2026). The VEGF/VEGFR axis in triple-negative breast cancer: A comprehensive review of therapeutic strategies. *Gene, 1001*, 150201. https://doi.org/10.1016/j.gene.2026.150201
2. Pourgholami, M. H., & Morris, D. L. (2008). Inhibitors of vascular endothelial growth factor in cancer. *Cardiovascular & Hematological Agents in Medicinal Chemistry, 6*(4), 343–347. https://doi.org/10.2174/187152508785909528
3. Kessenbrock, K., Plaks, V., & Werb, Z. (2010). Matrix metalloproteinases: Regulators of the tumor microenvironment. *Cell, 141*(1), 52–67. https://doi.org/10.1016/j.cell.2010.03.015
4. Vempati, P., Popel, A. S., & Mac Gabhann, F. (2014). Extracellular regulation of VEGF: Isoforms, proteolysis, and vascular patterning. *Cytokine & Growth Factor Reviews, 25*(1), 1–19. https://doi.org/10.1016/j.cytogfr.2013.11.002
5. Mondal, S., Adhikari, N., Banerjee, S., Amin, S. A., & Jha, T. (2020). Matrix metalloproteinase-9 (MMP-9) and its inhibitors in cancer: A minireview. *European Journal of Medicinal Chemistry, 194*, 112260. https://doi.org/10.1016/j.ejmech.2020.112260
6. Shoari, A., Coban, M. A., & Radisky, E. S. (2026). Therapeutic potential of inhibitors of gelatinases MMP-2 and MMP-9 for the treatment of breast cancer. *The FEBS Journal, 293*(13), 4014–4042. https://doi.org/10.1111/febs.70343
7. Fields, G. B. (2019). The rebirth of matrix metalloproteinase inhibitors: Moving beyond the dogma. *Cells, 8*(9), 984. https://doi.org/10.3390/cells8090984
8. Wu, X., Wang, J., Xia, S., Cheng, S., & Shi, Y. (2022). 1,2,3-Triazole derivatives with anti-breast cancer potential. *Current Topics in Medicinal Chemistry, 22*(17), 1406–1425. https://doi.org/10.2174/1568026622666220415225334
9. Arnaoutova, I., & Kleinman, H. K. (2010). *In vitro* angiogenesis: Endothelial cell tube formation on gelled basement membrane extract. *Nature Protocols, 5*(4), 628–635. https://doi.org/10.1038/nprot.2010.6
10. DeCicco-Skinner, K. L., Henry, G. H., Cataisson, C., Tabib, T., Gwilliam, J. C., Watson, N. J., Bullwinkle, E. M., Falkenburg, L., O'Neill, R. C., Morin, A., & Wiest, J. S. (2014). Endothelial cell tube formation assay for the *in vitro* study of angiogenesis. *Journal of Visualized Experiments, 91*, e51312. https://doi.org/10.3791/51312
11. Dixon, S. L., Smondyrev, A. M., & Rao, S. N. (2006). PHASE: A novel approach to pharmacophore modeling and 3D database searching. *Chemical Biology & Drug Design, 67*(5), 370–372. https://doi.org/10.1111/j.1747-0285.2006.00384.x

12. Knight, C. G., Willenbrock, F., & Murphy, G. (1992). A novel coumarin-labelled peptide for sensitive continuous assays of the matrix metalloproteinases. *FEBS Letters, 296*(3), 263–266. https://doi.org/10.1016/0014-5793(92)80300-6
13. Liang, C. C., Park, A. Y., & Guan, J. L. (2007). *In vitro* scratch assay: A convenient and inexpensive method for analysis of cell migration *in vitro*. *Nature Protocols, 2*(2), 329–333. https://doi.org/10.1038/nprot.2007.30
14. Mosmann, T. (1983). Rapid colorimetric assay for cellular growth and survival: Application to proliferation and cytotoxicity assays. *Journal of Immunological Methods, 65*(1–2), 55–63. https://doi.org/10.1016/0022-1759(83)90303-4
15. Neumann, U., Kubota, H., Frei, K., Ganu, V., & Leppert, D. (2004). Characterization of Mca-Lys-Pro-Leu-Gly-Leu-Dpa-Ala-Arg-NH_2, a fluorogenic substrate with increased specificity constants for collagenases and tumor necrosis factor converting enzyme. *Analytical Biochemistry, 328*(2), 166–173. https://doi.org/10.1016/j.ab.2003.12.035
16. Olsson, M. H. M., Søndergaard, C. R., Rostkowski, M., & Jensen, J. H. (2011). PROPKA3: Consistent treatment of internal and surface residues in empirical pKa predictions. *Journal of Chemical Theory and Computation, 7*(2), 525–537. https://doi.org/10.1021/ct100578z
17. Sastry, G. M., Adzhigirey, M., Day, T., Annabhimoju, R., & Sherman, W. (2013). Protein and ligand preparation: Parameters, protocols, and influence on virtual screening enrichments. *Journal of Computer-Aided Molecular Design, 27*(3), 221–234. https://doi.org/10.1007/s10822-013-9644-8